Design and Synthesis of Bubble-Nanorod-Structured Fe_2O_3—Carbon Nanofibers as Advanced Anode Material for Li-Ion Batteries

Jung Sang Cho, Young Jun Hong, and Yun Chan Kang*

Department of Materials Science and Engineering, Korea University, Anam-Dong, Seongbuk-Gu, Seoul 136-713, Republic of Korea

ABSTRACT A structure denoted as a "bubble-nanorod composite" is synthesized by introducing the Kirkendall effect into the electrospinning method. Bubble-nanorod-structured Fe_2O_3—C composite nanofibers, which are composed of nanosized hollow Fe_2O_3 spheres uniformly dispersed in an amorphous carbon matrix, are synthesized as the target material. Post-treatment of the electrospun precursor nanofibers at 500 °C under 10% H_2/Ar mixture gas atmosphere produces amorphous FeO_x—carbon composite nanofibers. Post-treatment of the FeO_x—carbon composite nanofibers at 300 °C under air atmosphere produces the bubble-nanorod-structured Fe_2O_3—C composite nanofibers. The solid Fe nanocrystals formed by the reduction of FeO_x are converted into hollow Fe_2O_3 nanospheres during the further heating process by the well-known Kirkendall diffusion process. The discharge capacities of the bubble-nanorod-structured Fe_2O_3—C composite nanofibers and hollow bare Fe_2O_3 nanofibers for the 300th cycles at a current density of 1.0 A g^{-1} are 812 and 285 mA h g^{-1}, respectively, and their capacity retentions measured from the second cycle are 84 and 24%, respectively. The hollow nanospheres accommodate the volume change that occurs during cycling. The unique structure of the bubble-nanorod-structured Fe_2O_3—C composite nanofibers results in their superior electrochemical properties by improving the structural stability during long-term cycling.

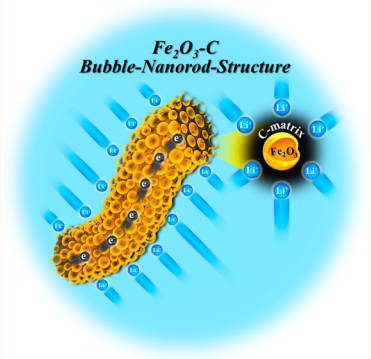

KEYWORDS: bubble nanorod · nanofibers · electrospinning · lithium ion battery · carbon composite

High energy density, high rate capability, and long cycle life are essential properties of Li-ion batteries (LIBs) for future electric vehicles and renewable energy storage.[1−7] To enhance these properties, numerous types of anode structures have been explored using various synthetic methods. Among these, one-dimensional (1-D) materials are becoming increasingly important in electrochemical energy conversion and storage devices, and hence they have attracted significant interest in recent years.[7−15] These 1-D structures have advantages such as large exposed surfaces and short diffusion lengths for lithium ions and direct channels for efficient electron transport, which enable the materials to interact more efficiently with Li^+ ions, resulting in high power density.

The electrospinning method is a simple and highly versatile method for the preparation of 1-D nanostructures. Therefore, various transition metal oxides (*e.g.*, Mn_xO_y, Ni_xO_y, FeO_x, Cu_xO_y, CoO_x, *etc.*), which possess high theoretical specific capacities, in the shapes of wires, fibers, tubes, and fiber-in-tube and tube-in-tube have been studied as potential next-generation electrode materials.[16−25] Mou *et al.* prepared maghemite (γ-Fe_2O_3) fiber-in-tube and tube-in-tube materials by controlling the heating rate of electrospun precursor fibers.[23] Lang *et al.* prepared solid, hollow, and tube-in-tube porous nanofiber TiO_2 structures by a simple non-coaxial electrospinning method from precursor solutions, with different concentrations of tetrabutyl titanate used as the Ti component.[24] Chen *et al.* introduced a multifluidic coaxial electrospinning approach to fabricate nanowire-in-microtube structures.[25]

Nanostructured Fe_2O_3 materials have been widely studied as anode materials for LIBs due to their high theoretical capacity

* Address correspondence to yckang@korea.ac.kr.

Received for review January 6, 2015 and accepted March 13, 2015.

Published online March 13, 2015
10.1021/acsnano.5b00088

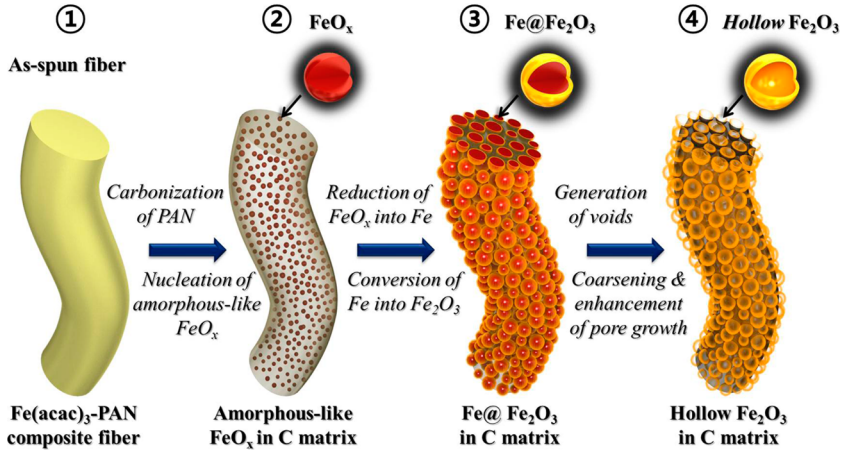

Scheme 1. Formation mechanism of bubble-nanorod-structured Fe_2O_3–C composite nanofiber by Kirkendall-type diffusion.

value (1005 mA h g^{-1}), low cost, natural abundance, and environmentally friendly nature.[7,19,20,26–30] Unfortunately, the commercial application of Fe_2O_3 for anodes in current LIBs is hindered by the rapid capacity fading during cycling, resulting from the low intrinsic electric and the large volume expansion.[26] To overcome these, the interstation of void space into the structure has been approached, which allows for the effective accommodation of mechanical stress during cycling, the decreased diffusion length, and increased contact area between the electrolyte and electrode for Li^+ insertion/desertion, thus leading to improved lithium storage properties.[31–33] The Kirkendall effect has been applied in the liquid solution process to prepare the hollow nanopowders.[33–35] However, to the best of our knowledge, the hollow Fe_2O_3 powders prepared by applying the Kirkendall diffusion process have not yet been researched as anode materials in LIBs.

Herein, we propose for the first time a novel Fe_2O_3 structure, denoted as a "bubble-nanorod" structure, which consists of nanofibers composed of nanosized hollow Fe_2O_3 spheres uniformly dispersed in an amorphous carbon matrix. The unique structure of the bubble-nanorod composite not only has advantages as a 1-D material but also allows for the effective accommodation of mechanical stress by means of the void spaces within the Fe_2O_3 bubbles and the presence of the surrounding carbon atoms. Simultaneously, carbon inhibits the aggregation of Fe_2O_3 nanoparticles and thus maintains the structural and electrical integrity of the composite during repeated charge and discharge processes. The bubble-nanorod structure therefore is ideal for use for LIB electrodes. The formation mechanism of the bubble-nanorod structure was investigated in detail by tracing each step of the synthetic process; the electrochemical performance of the bubble-nanorod-structured Fe_2O_3–C composite was also evaluated. Our findings are expected to be very useful for the design and synthesis of novel intermetallic compounds as advanced anode materials for Li-ion batteries.

RESULTS AND DISCUSSION

The formation of the bubble-nanorod-structured Fe_2O_3–C nanofibers is described in Scheme 1. Composite nanofibers consisting of iron acetylacetonate [$Fe(acac)_3$] and polyacrylonitrile (PAN) were prepared by the electrospinning process (Scheme 1, ①). Post-treatment of the electrospun precursor nanofibers at 500 °C under H_2/Ar mixture gas atmosphere produced amorphous FeO_x–carbon composite nanofibers. The carbonization of PAN and the decomposition of iron acetylacetonate produced FeO_x-carbon composite nanofibers (Scheme 1, ②). The large amount of carbon in the fiber disturbed the crystal growth of FeO_x. The subsequent post-treatment of the FeO_x–carbon composite nanofibers at 300 °C under air atmosphere produced the bubble-nanorod-structured Fe_2O_3–C composite nanofiber. Reduction of FeO_x crystals surrounded by the carbon matrix into Fe metal occurred during the post-treatment under air atmosphere by the following equation: $FeO_x(s) + xC(s) \rightarrow Fe(s) + xCO(g)$. The crystal growth of Fe formed ultrafine Fe nanocrystals uniformly dispersed within the carbon nanofibers during the early stage of post-treatment by the consumption of some amount of carbon. The solid Fe nanocrystals were converted into hollow Fe_2O_3 nanospheres during the subsequent heating process by the well-known Kirkendall effect. The Kirkendall effect, a vacancy flux and subsequent void formation process resulting from diffusivity differences at inorganic interfaces, was first reported by Aldinger.[33] The Kirkendall effect results in the formation of a thin Fe_2O_3 layer on the Fe metal surface (Scheme 1, ③), followed by simultaneous outward diffusion of Fe cations through the oxide layer and inward diffusion of oxygen into the nanospheres, creating an intermediate $Fe@Fe_2O_3$ core–shell structure (Scheme 2b). Fe cations diffused outward more quickly than oxygen diffused

inward, which is consistent with the larger ionic radius of oxygen anions (140 pm) than Fe cations (Fe^{2+} is 76 pm, Fe^{3+} is 65 pm). Accordingly, Kirkendall voids were generated near the Fe/Fe_2O_3 interface during vacancy-assisted exchange of the material *via* bulk interdiffusion (Scheme 2c), which gave rise to coarsening and enhancement of pore growth in the spheres (Scheme 1, ④). Complete conversion of Fe metal into Fe_2O_3 by Kirkendall-type diffusion resulted in the bubble-nanorod-structured Fe_2O_3—C composite nanofibers.

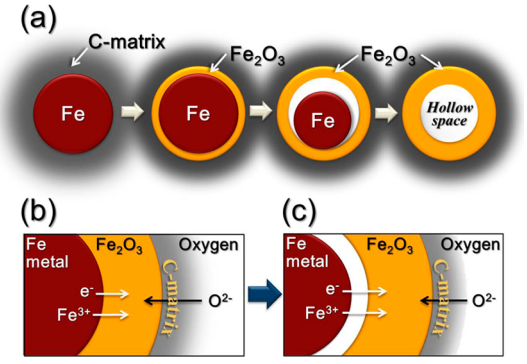

Scheme 2. (a) Formation mechanism of hollow Fe_2O_3 nanosphere in the bubble-nanorod-structured Fe_2O_3—carbon composite nanofiber by Kirkendall effect. (b,c) Its chemical conversion process in the surface region of a sphere.

The formation mechanism of the bubble-nanorod-structured Fe_2O_3—C nanofiber was investigated on the basis of post-treatment-induced morphology changes in the electrospun precursor nanofibers. The morphologies of the nanofibers post-treated at 500 °C under H_2/Ar mixture gas atmosphere are shown in Figure 1. The TEM images do not show a crystal phase within the nanofibers. The selected area electron diffraction (SAED) pattern shown in Figure 1c also shows the amorphous structure of the nanofibers. The elemental mapping images shown in Figure 1d reveal the uniform distribution of Fe, O, and C throughout the nanofibers. Fe is mainly present as an amorphous FeO_x phase within the carbon nanofibers, which is proved by observing the Fe—O functional group at 529.6 eV in the XPS result (Supporting Information, Figure S1). Nevertheless, the crystal phase of Fe_3C was only confirmed from the phase analysis in Supporting Information, Figure S2. It is because FeO_x nuclei in the amorphous FeO_x—C composite nanofiber were partially reduced to Fe metal, and then Fe_3C phase formed in the part of Fe surface encountered with carbon (Supporting Information, Figure S3).

The morphologies of the bubble-nanorod-structured Fe_2O_3—C composite nanofibers are shown in Figure 2. The low-resolution SEM and TEM images shown in Figure 2a,b reveal the uniform structure of the

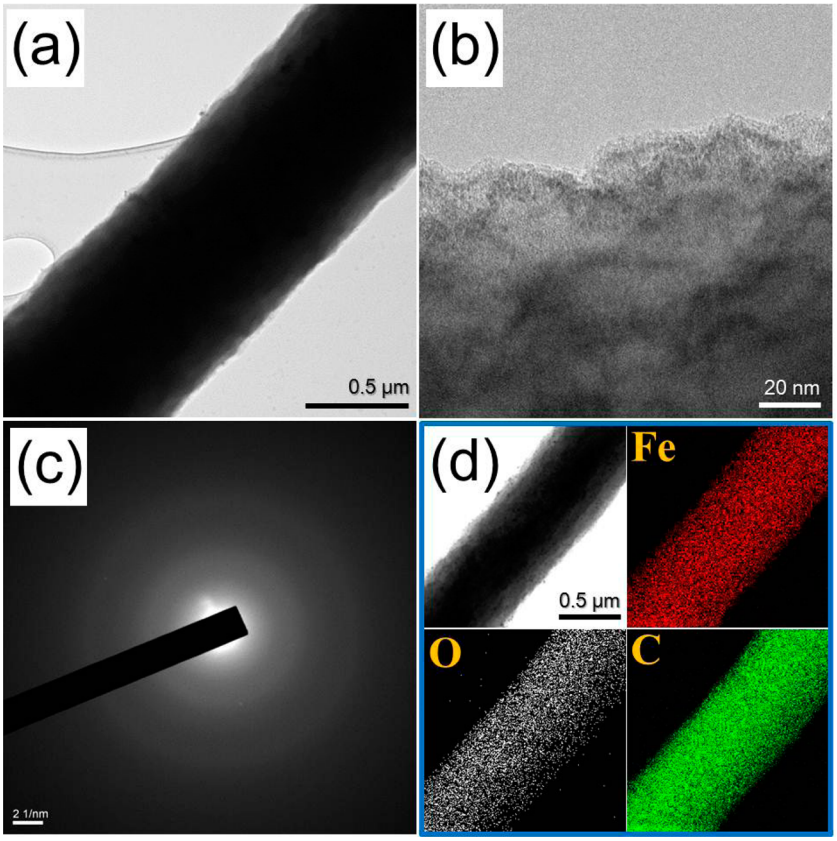

Figure 1. Morphologies, SAED, and elemental mapping images of the nanofibers post-treated at 500 °C under H_2/Ar mixed gas atmosphere: (a,b) TEM images, (c) SAED pattern, and (d) elemental mapping images.

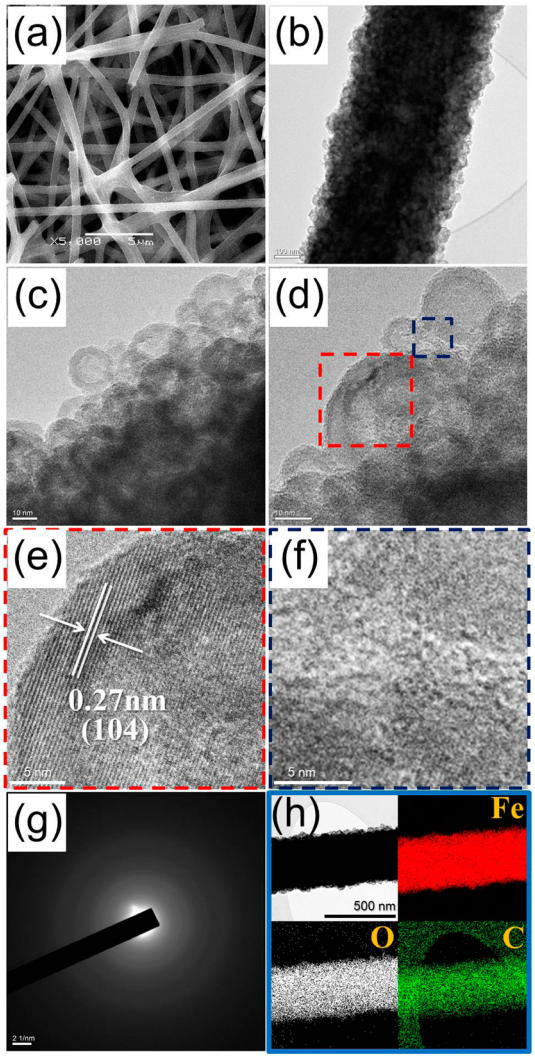

Figure 2. Morphologies and elemental mapping images of the bubble-nanorod-structured Fe_2O_3–C composite nanofibers: (a) SEM image, (b–d) TEM images, (e,f) HR-TEM images, (g) SAED pattern, and (h) elemental mapping images.

nanofibers. The smooth surface of the nanofibers became rough after post-treatment under air atmosphere owing to the formation of hollow Fe_2O_3 nanospheres. The high-resolution (HR) TEM images shown in Figure 2c,d show hollow Fe_2O_3 nanospheres uniformly dispersed within the carbon nanofibers. The mean size of the hollow nanospheres measured from the HR-TEM images was 17 nm. The mean shell thickness of the hollow nanospheres was 3.0 nm. The enlarged TEM image (Figure 2e) of the region marked with a large rectangle in Figure 2d shows clear lattice fringes separated by 0.27 nm, which correspond to the (104) lattice plane of Fe_2O_3. The enlarged TEM image (Figure 2f) of the region marked with a small rectangle in Figure 2d showing the space surrounded with hollow nanospheres shows the amorphous carbon layer. The SAED pattern, shown in Figure 2g, reveals the amorphous structure of the bubble-nanorod-structured Fe_2O_3–C nanofibers resulting from the ultrafine nanocrystals of Fe_2O_3. The elemental mapping images shown in Figure 2h reveal the uniform distribution of hollow Fe_2O_3 nanospheres and carbon throughout the bubble-nanorod-structured Fe_2O_3–C nanofibers. The existence of Fe_2O_3 and carbon in the structure was further confirmed by observing the peaks of Fe 2p, O 1s, and C 1s from the XPS spectra in Supporting Information, Figure S1.

The morphologies of the bare Fe_2O_3 nanofibers formed by direct post-treatment of the electrospun nanofibers at 500 °C under air atmosphere are shown in Figure 3. The direct decomposition of [Fe(acac)$_3$] into Fe_2O_3 and complete decomposition of PVP into gases resulted in the fabrication of Fe_2O_3 nanofibers. The SEM and TEM images shown in Figure 3a,b reveal the hollow structure of the Fe_2O_3 nanofibers. Porous and filled Fe_2O_3 nanofibers were first formed as an intermediate product during the heat-treatment process. However, Ostwald ripening changed the filled Fe_2O_3 nanofibers into hollow nanofibers. The HR-TEM images shown in Figure 3c,d indicate well-grown Fe_2O_3 crystals during the post-treatment process. The enlarged TEM image shown in Figure 3d shows clear lattice fringes separated by 0.25 nm, which correspond to the (110) lattice plane of Fe_2O_3. The SAED pattern shown in Figure 3e also reveals the highly crystalline structure of the hollow Fe_2O_3 nanofibers. The elemental mapping images shown in Figure 3f show the trace amounts of carbon present in the nanofibers.

The XRD patterns of the bubble-nanorod-structured Fe_2O_3–C composite and hollow bare Fe_2O_3 nanofibers are shown in Figure 4a. The bare Fe_2O_3 nanofibers have sharp XRD peaks, indicating a large mean crystallite size. However, the XRD pattern of the bubble-nanorod-structured Fe_2O_3–C composite nanofibers shows peaks of Fe_2O_3 phase with small intensities. The hollow Fe_2O_3 nanospheres with a shell thickness of 3.0 nm were composed with ultrafine nanocrystals. The Raman spectrum of the bubble-nanorod-structured Fe_2O_3–C composite nanofibers shown in Figure 4b contains characteristic wide D and G bands of carbon at approximately 1350 and 1590 cm^{-1}, respectively. The peak intensity ratio between the D and G bands (I_D/I_G) generally provides a useful index for comparing the degree of crystallinity of carbon materials, *i.e.*, the smaller the ratio of I_D/I_G, the higher the degree of ordering in the carbon material.[36−39] The I_D/I_G ratio was found to be 2.16, demonstrating that the carbon formed in this specimen was fairly disordered, that is, amorphous hard carbon. The thermogravimetric (TG) curve of the bubble-nanorod-structured Fe_2O_3–C composite nanofibers is shown in Figure 4c. A strict weight loss was observed in the TG curve from 320 °C onward owing to the degradation of amorphous carbon. The carbon content of the bubble-nanorod-structured Fe_2O_3–C composite nanofibers estimated from the TG analysis was 38 wt %. The BET surface areas

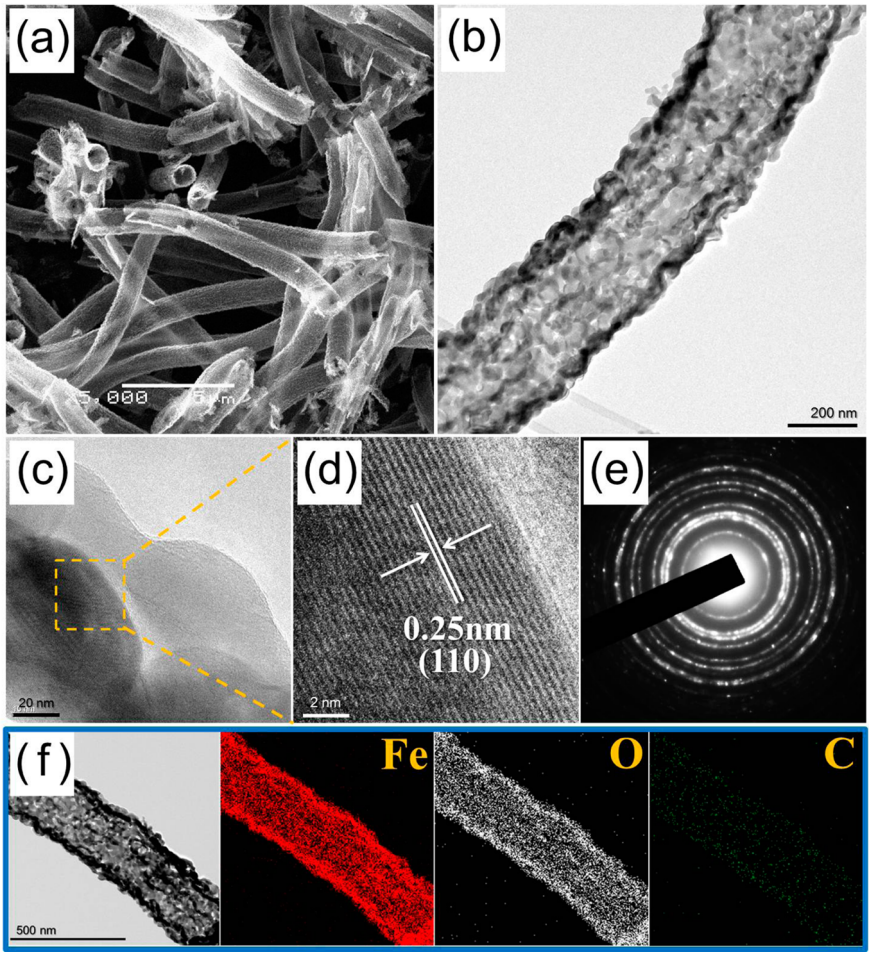

Figure 3. Morphologies and elemental mapping images of bare Fe_2O_3 hollow nanofibers formed by direct post-treatment of the electrospun nanofibers at 500 °C under air atmosphere: (a) SEM image, (b,c) TEM image, (d) HR-TEM image, (e) SAED pattern, and (f) elemental mapping images.

of the bubble-nanorod-structured Fe_2O_3−C composite and hollow bare Fe_2O_3 nanofibers were 32 and 40 $m^2\ g^{-1}$, respectively, in Supporting Information, Figure S4.

The electrochemical properties of the bubble-nanorod-structured Fe_2O_3−C composite nanofibers were compared with those of the hollow bare Fe_2O_3 nanofibers and the results are shown in Figure 5. The cyclic voltammogram (CV) curves of the bubble-nanorod-structured Fe_2O_3−C composite nanofibers for the first six cycles at a scan rate of 0.1 mV s^{-1} are shown in Figure 5a. A well-defined reduction peak is observed at 0.7 V *vs* Li^+/Li, which was ascribed to the complete reduction of Fe(III) to Fe(0), the formation of Li_2O, and the irreversible reductive reaction of the electrolyte to form a solid electrolyte interphase (SEI) film.[40,41] In the first anodic scan, the two broad overlapping oxidation peaks at 1.5 and 1.8 V correspond to the reversible oxidation of Fe(0) to Fe(II) and Fe(II) to Fe(III), respectively.[42−45] The oxidation peak at 1.05 V can be attributed to the partial decomposition of SEI.[46] For the second cycle, one reduction peak appears at 0.8 V with decreased intensity, whereas two oxidation peaks remained unchanged, indicating irreversible phase transformation with the formation of an SEI film in the first cycle and good reversible reactions of Fe(0) to Fe(II) and Fe(II) to Fe(III), respectively.[47−50] The good overlapping of the CV curves from the fourth cycle onward reveals good reversibility of the electrochemical reactions.

The initial charge and discharge curves of the two samples at a constant current density of 1 A g^{-1} are shown in Figure 5b. The initial discharge curve of the hollow bare Fe_2O_3 nanofibers shows two plateaus near 1.5 and 1.0 V due to lithium insertion into α-Fe_2O_3 without a structural change and the phase transformation from hexagonal α-$Li_xFe_2O_3$ to cubic $Li_xFe_2O_3$.[7,20,51] However, clear plateaus near 1.5 and 1.0 V are not observed in the initial discharge curve of the bubble-nanorod-structured Fe_2O_3−C composite nanofibers owing to their ultrafine crystallite size. Typically, the anode materials with amorphous phase or ultrafine nanocrytals exhibit slope charge/discharge profiles, while crystal materials present flat plateaus.[52−54] In the two samples, a long plateau at approximately 0.7 V resulting from the complete reduction of Fe(III) to Fe(0)

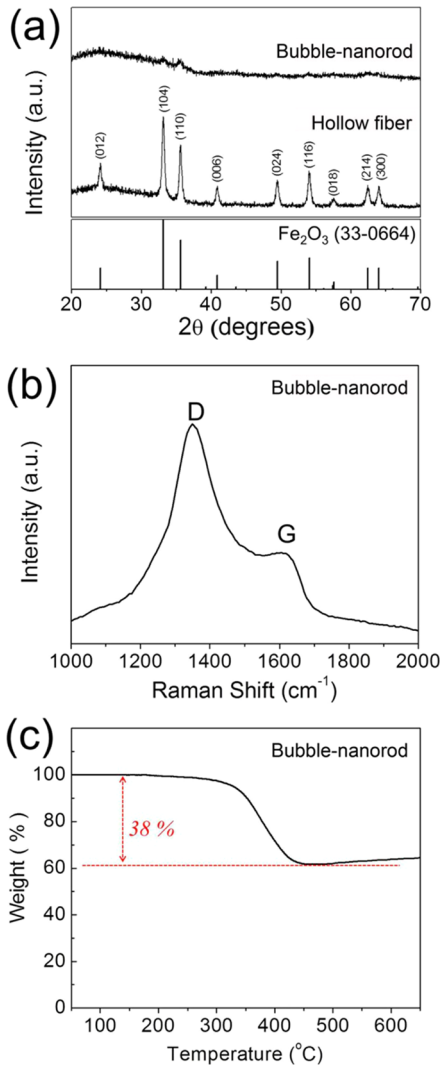

Figure 4. (a) XRD patterns of bare Fe_2O_3 hollow nanofibers and bubble-nanorod-structured Fe_2O_3—C composite nanofibers. (b) Raman spectrum and (c) thermal analysis of bubble-nanorod-structured Fe_2O_3—C composite nanofibers.

is observed in the initial discharge curves.[45,55,56] The initial discharge and charge capacities of the hollow bare Fe_2O_3 and bubble-nanorod-structured Fe_2O_3—C composite nanofibers were 1406 and 1145 mA h g^{-1}, and 1385 and 957 mA h g^{-1} respectively, and their corresponding initial Columbic efficiencies were 81 and 69%, respectively. The initial irreversible capacity loss of the bare Fe_2O_3 nanofibers is ascribed to the formation of an SEI layer on the surface of the nanofibers and the incomplete restoration of metallic Fe into the original oxide during the initial charging process.[20,57] The high amount of amorphous carbon, which has a low lithium storage capacity and a large initial irreversible capacity loss, decreased the initial discharge capacity and Columbic efficiency of the bubble-nanorod-structured Fe_2O_3—C composite fibers.[58,59]

The long-term cycling performance of the two samples at a constant current density of 1.0 A g^{-1} is

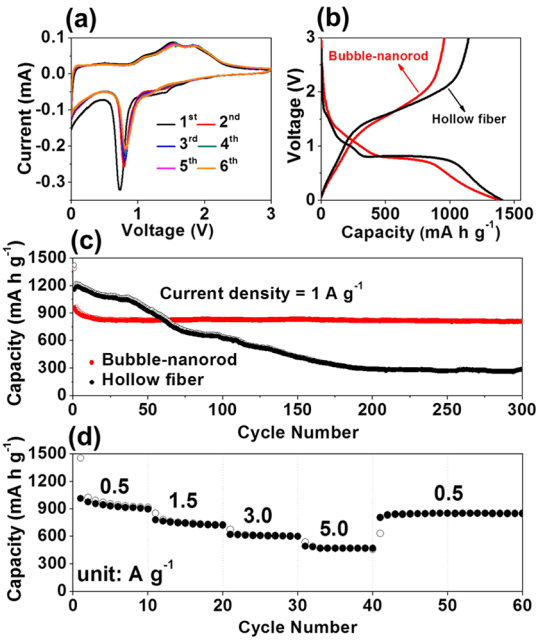

Figure 5. Electrochemical properties of bare Fe_2O_3 hollow nanofibers and bubble-nanorod-structured Fe_2O_3—C composite nanofibers: (a) CV curves of bubble-nanorod-structured nanofibers, (b) first charge—discharge curves, (c) cycling performances, and (d) rate performance of bubble-nanorod-structured nanofibers.

shown in Figure 5c. The discharge capacities of the bubble-nanorod-structured Fe_2O_3—C composite nanofibers decreased slightly from 968 to 824 mA h g^{-1} during the first 30 cycles from the second cycle; the discharge capacity then remained constant during the further 270 cycles. The initial capacity loss of the bubble-nanorod-structured Fe_2O_3—C composite nanofibers was attributed to the partial destruction of the internal structure, the irreversible electrochemical decomposition of electrolyte and the subsequent formation of a SEI layer on the surface.[30,60,61] However, the discharge capacities of the hollow bare Fe_2O_3 nanofibers decreased steadily from the second cycle during the first 210 cycles. The discharge capacities of the bubble-nanorod-structured Fe_2O_3—C composite and hollow bare Fe_2O_3 nanofibers for the 300th cycles were 812 and 284 mA h g^{-1}, respectively and their capacity retentions measured from the second cycle were 84 and 24%, respectively. The rate performance of the bubble-nanorod-structured Fe_2O_3—C composite nanofibers is shown in Figure 5d, in which current density was increased stepwise from 0.5 to 5.0 A g^{-1} for every 10 successive cycles in the voltage range of 0.001—3.0 V. The stable reversible discharge capacities of the nanofibers decreased from 913 to 491 mA h g^{-1} as the current density increased from 0.5 to 5.0 A g^{-1}. Furthermore, the discharge capacity recovered to 852 mA h g^{-1} as the current density was restored to 0.5 A g^{-1}.

Electrochemical impedance spectroscopy (EIS) measurements were carried out to explain the superior

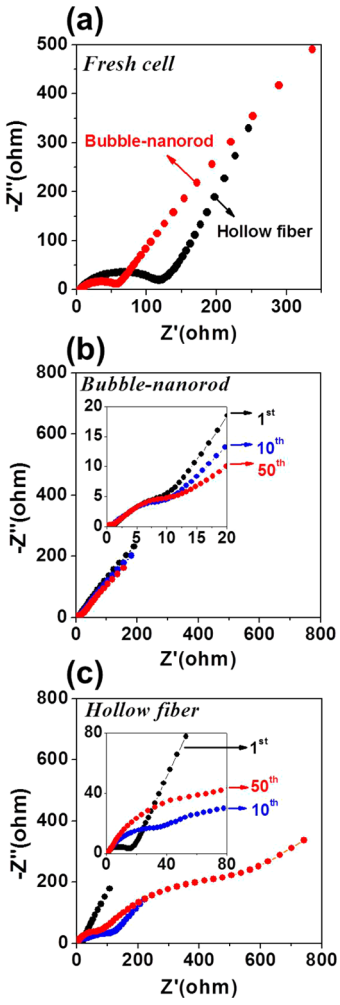

Figure 6. Impedance analysis of bare Fe_2O_3 hollow nanofibers and bubble-nanorod-structured Fe_2O_3–C composite nanofibers: (a) before cycling, (b) after cycling for bubble-nanorod-structured nanofibers, and (c) after cycling for hollow nanofibers.

cycling and rate performance of the bubble-nanorod-structured Fe_2O_3–C composite nanofibers. The Nyquist impedance plots of the bubble-nanorod-structured Fe_2O_3–C composite and hollow bare Fe_2O_3 nanofibers obtained before and after cycling under a fully charged state are shown in Figure 6. The medium-frequency semicircles in the Nyquist plots of the electrodes are assigned to the charge-transfer resistance (R_{ct}).[61–63] The bubble-nanorod-structured Fe_2O_3–C composite nanofibers with ultrafine nanocrystals of a few nanometers in size had a lower charge-transfer resistance than the hollow bare Fe_2O_3 nanofibers with a large crystallite size of 41 nm before cycling, as shown in Figure 6a. The charge-transfer resistance of the two samples decreased after the first cycling owing to the formation of an amorphous structure, as shown in Figure 6b,c.[64–66] The charge-transfer resistance of the bubble-nanorod-structured Fe_2O_3–C composite nanofibers changed slightly during the first 50 cycles, as shown in Figure 6b. However, the charge-transfer resistance of the hollow bare Fe_2O_3 nanofibers increased abruptly with increasing cycle number, as shown in Figure 6c. The destruction of the hollow bare Fe_2O_3 nanofibers during cycling decreased the electrical contact with the copper foil electrode (Supporting Information, Figure S5). The hollow structure of the nanospheres dispersed in the carbon nanofibers was well maintained even after repeated lithium insertion and desertion processes at a high current density of 1.0 A g^{-1} (Figure S5). The void space of the hollow nanosphere accommodates the volume change during the cycling process. Therefore, the unique structure of the bubble-nanorod-structured Fe_2O_3–C composite nanofibers resulted in their superior electrochemical properties by improving the structural stability during long-term cycling.

CONCLUSIONS

We propose the synthesis of a newly designed nanostructured material, denoted as "bubble-nanorod-structured Fe_2O_3–C composite nanofibers". The electrospun precursor nanofibers were turned into the novel-structured Fe_2O_3–C composite nanofibers by a simple two-step post-treatment process under respective H_2/Ar and air atmospheres. The Kirkendall effect played a key role in the formation of the bubble-nanorod-structured Fe_2O_3–C composite nanofibers. However, a single-step post-treatment process of the electrospun nanofibers under air atmosphere alone produced the hollow bare Fe_2O_3 nanofibers. The bubble-nanorod-structured Fe_2O_3–C nanofibers showed superior electrochemical properties as an anode material for LIBs as compared with the hollow bare Fe_2O_3 nanofibers. The synergetic effect of hollow nanospheres and a carbon matrix resulted in the superior cycling and rate performance of the bubble-nanorod-structured Fe_2O_3–C nanofibers. The simple synthesis method could be widely applied in the preparation of bubble-nanorod-structured metal oxide–C composites and metal oxide nanofibers for a wide range of applications, including energy storage.

EXPERIMENTAL SECTION

Sample Preparation. $Fe(acac)_3$–PAN composite nanofibers were prepared by electrospinning. The precursor solution for electrospinning was prepared by dissolving 4 g of $Fe(acac)_3$ and 4 g of PAN (M_w = 150 000) in 50 mL of *N*,*N*-dimethylformamide (DMF) with vigorously stirring overnight. The prepared solution was loaded at a flow rate of 10 mL h^{-1} into a plastic syringe equipped with a 25-gauge stainless steel nozzle. The solution was then ejected and electrospun onto a drum collector covered with aluminum foil. The distance between the tip and the collector was kept constant at 20 cm and the rotation of the

drum was maintained at 100 rpm during the electrospinning process. The applied voltage between the collector and the syringe tip was 25 kV. The resultant Fe(acac)$_3$—PAN composite nanofibers were stabilized at 220 °C in air for 1 h. For the bubble-nanorod-structured Fe_2O_3—C composite nanofibers, post-treatment was carried out at 500 °C in the presence of a 10% H_2/Ar mixture gas for 3 h. The nanofibers were subsequently treated at 300 °C in air for 3 h. For the comparison bare sample, hollow Fe_2O_3 nanofibers without carbon were also prepared by post-treatment of as-spun Fe(acac)$_3$—PAN composite nanofibers at 500 °C in air atmosphere for 3 h.

Characterization Techniques. The microstructures of the nanofibers were observed by field-emission scanning electron microscopy (FE-SEM, S-4800, Hitachi) and field-emission transmission electron microscopy (FE-TEM, JEM-2100F, JEOL). In addition, their crystal phases were evaluated by X-ray diffractometry (XRD, X'Pert PRO MPD) using Cu Kα radiation (λ = 1.5418 Å) at the Korea Basic Science Institute (Daegu). The structural characterization of the carbon in the specimens was performed by Raman spectra (Jobin Yvon LabRam HR800, excited by 632.8 nm He—Ne laser) at room temperature. X-ray photoelectron spectroscopy (XPS, Thermo Scientific K-Alpha) with a focused monochromatic Al Kα at 12 kV and 20 mA was used to analyze the composition of the specimens. The surface areas of the nanofibers were measured by the Brunauer—Emmett—Teller (BET) method, using N_2 as the adsorbate gas. Thermogravimetric analysis was performed using a Pyris 1 TGA (Perkin Elmer) within a temperature range of 25—650 °C and at a heating rate of 10 °C min^{-1} under static air atmosphere.

Electrochemical Measurements. The electrochemical properties of the nanofibers were analyzed by constructing a 2032-type coin cell. The anode was prepared by mixing the active material, carbon black, and sodium carboxymethyl cellulose (CMC) in a weight ratio of 7:2:1. Li metal and microporous polypropylene film were used as the counter electrode and the separator, respectively. The electrolyte was 1 M $LiPF_6$ dissolved in a mixture of ethylene carbonate/dimethyl carbonate (EC/DMC; 1:1 v/v). The discharge/charge characteristics of the samples were investigated by cycling in the 0.001—3 V potential range at various current densities. CVs were measured at a scan rate of 0.1 mV s^{-1}. The size of the Fe_2O_3 nanofibers negative electrode was 1 cm × 1 cm, and the mass loading was approximately 1.2 mg cm^{-2}.

Conflict of Interest: The authors declare no competing financial interest.

Supporting Information Available: XPS spectra of the Fe_2O_3 nanofibers; XRD patterns of the Fe_2O_3 nanofibers; TEM and HR-TEM images of the Fe_2O_3 nanofibers; N_2 gas adsorption and desorption isotherms and pore size distribution of the Fe_2O_3 nanofibers; TEM images of the Fe_2O_3 nanofibers obtained after 300 cycles; SEM image of electrospun nanofibers; TG analysis of the Fe_2O_3 nanofibers; FE-SEM image of bubble-rod-structured Fe_2O_3—C composite nanofibers; digital photos and SEM images of the nanofibers obtained at different post-treatment temperatures under air; electrochemical properties of the bubble-nanorod-structured Fe_2O_3—C composite nanofibers using the anode prepared by mixing the active material, carbon black, and sodium carboxymethyl cellulose (CMC) in a weight ratio of 8:1:1; and electrochemical properties of FeO_x—carbon composite nanofibers after thermal treatment at 500 °C under H_2/Ar gas atmosphere. This material is available free of charge *via* the Internet at http://pubs.acs.org.

Acknowledgment. This work was supported by the National Research Foundation of Korea (NRF) grant funded by the Korea government (MEST) (No. 2012R1A2A2A02046367).

REFERENCES AND NOTES

1. Gogotsi, Y. What Nano Can Do for Energy Storage. *ACS Nano* **2014**, *8*, 5369–5371.
2. Liu, C.; Li, F.; Ma, L. P.; Cheng, H. M. Advanced Materials for Energy Storage. *Adv. Mater.* **2010**, *22*, E28–E62.
3. Lou, X. W.; Li, C. M.; Archer, L. A. Designed Synthesis of Coaxial SnO_2@Carbon Hollow Nanospheres for Highly Reversible Lithium Storage. *Adv. Mater.* **2009**, *21*, 2536–2539.
4. Er, D.; Li, J.; Naguib, M.; Gogotsi, Y.; Shenoy, V. B. Ti_3C_2 MXene as a High Capacity Electrode Material for Metal (Li, Na, K, Ca) Ion Batteries. *ACS Appl. Mater. Interfaces* **2014**, *6*, 11173–11179.
5. Yuan, S. M.; Li, J. X.; Yang, L. T.; Su, L. W.; Liu, L.; Zhou, Z. Preparation and Lithium Storage Performances of Mesoporous Fe_3O_4@C Microcapsules. *ACS Appl. Mater. Interfaces* **2011**, *3*, 705–709.
6. Wang, L.; Tang, W.; Jing, Y.; Su, L.; Zhou, Z. Do Transition Metal Carbonates Have Greater Lithium Storage Capability Than Oxides? A Case Study of Monodisperse $CoCO_3$ and CoO Microspindles. *ACS Appl. Mater. Interfaces* **2014**, *6*, 12346–12352.
7. Chen, J.; Xu, L. N.; Li, W. Y.; Gou, X. L. α-Fe_2O_3 Nanotubes in Gas Sensor and Lithium-Ion Battery Applications. *Adv. Mater.* **2005**, *17*, 582–586.
8. Chen, J.; Xia, X. H.; Tu, J. P.; Xiong, Q. Q.; Yu, Y. X.; Wang, X. L.; Gu, C. D. Co_3O_4—C Core—Shell Nanowire Array as an Advanced Anode Material for Lithium Ion Batteries. *J. Mater. Chem.* **2012**, *22*, 15056–15061.
9. Gao, X. P.; Bao, J. L.; Pan, G. L.; Zhu, H. Y.; Huang, P. X.; Wu, F.; Song, D. Y. Preparation and Electrochemical Performance of Polycrystalline and Single Crystalline CuO Nanorods as Anode Materials for Li Ion Battery. *J. Phys. Chem. B* **2004**, *108*, 5547–5551.
10. Ge, M.; Rong, J.; Fang, X.; Zhou, C. Porous Doped Silicon Nanowires for Lithium Ion Battery Anode with Long Cycle Life. *Nano Lett.* **2012**, *12*, 2318–2323.
11. Jiang, J.; Li, Y.; Liu, J.; Huang, X. Building One-Dimensional Oxide Nanostructure Arrays on Conductive Metal Substrates for Lithium-Ion Battery Anodes. *Nanoscale* **2011**, *3*, 45–58.
12. Kim, D. W.; Hwang, I. S.; Kwon, S. J.; Kang, H. Y.; Park, K. S.; Choi, Y. J.; Choi, K. J.; Park, J. G. Highly Conductive Coaxial SnO_2—In_2O_3 Heterostructured Nanowires for Li Ion Battery Electrodes. *Nano Lett.* **2007**, *7*, 3041–3045.
13. Xu, W.; Zhao, K.; Niu, C.; Zhang, L.; Cai, Z.; Han, C.; He, L.; Shen, T.; Yan, M.; Qu, L.; ; *et al.* Heterogeneous Branched Core—Shell SnO_2—PANI Nanorod Arrays with Mechanical Integrity and Three Dimentional Electron Transport for Lithium Batteries. *Nano Energy* **2014**, *8*, 196–204.
14. Zhang, G.; Yu, L.; Hoster, H. E.; Lou, X. W. Synthesis of One-Dimensional Hierarchical NiO Hollow Nanostructures with Enhanced Supercapacitive Performance. *Nanoscale* **2013**, *5*, 877–881.
15. Niu, C.; Meng, J.; Han, C.; Zhao, K.; Yan, M.; Mai, L. VO_2 Nanowires Assembled into Hollow Microspheres for High-Rate and Long-Life Lithium Batteries. *Nano Lett.* **2014**, *14*, 2873–2878.
16. Aravindan, V.; Suresh Kumar, P.; Sundaramurthy, J.; Ling, W. C.; Ramakrishna, S.; Madhavi, S. Electrospun NiO Nanofibers as High Performance Anode Material for Li-Ion Batteries. *J. Power Sources* **2013**, *227*, 284–290.
17. Barakat, N. A. M.; Khil, M. S.; Sheikh, F. A.; Kim, H. Y. Synthesis and Optical Properties of Two Cobalt Oxides (CoO and Co_3O_4) Nanofibers Produced by Electrospinning Process. *J. Phys. Chem. C* **2008**, *112*, 12225–12233.
18. Cavaliere, S.; Subianto, S.; Savych, I.; Jones, D. J.; Rozière, J. Electrospinning: Designed Architectures for Energy Conversion and Storage Devices. *Energy Environ. Sci.* **2011**, *4*, 4761–4785.
19. Chaudhari, S.; Srinivasan, M. 1D Hollow α-Fe_2O_3 Electrospun Nanofibers as High Performance Anode Material for Lithium Ion Batteries. *J. Mater. Chem.* **2012**, *22*, 23049–23056.
20. Cherian, C. T.; Sundaramurthy, J.; Kalaivani, M.; Ragupathy, P.; Kumar, P. S.; Thavasi, V.; Reddy, M.; Sow, C. H.; Mhaisalkar, S. G.; Ramakrishna, S. Electrospun α-Fe_2O_3 Nanorods as a Stable, High Capacity Anode Material for Li-Ion Batteries. *J. Mater. Chem.* **2012**, *22*, 12198–12204.
21. Fan, Q.; Whittingham, M. S. Electrospun Manganese Oxide Nanofibers as Anodes for Lithium-Ion Batteries. *Electrochem. Solid-State Lett.* **2007**, *10*, A48–A51.

22. Sahay, R.; Suresh Kumar, P.; Aravindan, V.; Sundaramurthy, J.; Chui Ling, W.; Mhaisalkar, S. G.; Ramakrishna, S.; Madhavi, S. High Aspect Ratio Electrospun CuO Nanofibers as Anode Material for Lithium-Ion Batteries with Superior Cycleability. *J. Phys. Chem. C* **2012**, *116*, 18087–18092.
23. Mou, F.; Guan, J. G.; Shi, W.; Sun, Z.; Wang, S. Oriented Contraction: A Facile Nonequilibrium Heat-Treatment Approach for Fabrication of Maghemite Fiber-in-Tube and Tube-in-Tube Nanostructures. *Langmuir* **2010**, *26*, 15580–15585.
24. Lang, L.; Wu, D.; Xu, Z. Controllable Fabrication of TiO_2 1D-Nano/Micro Structures: Solid, Hollow, and Tube-in-Tube Fibers by Electrospinning and the Photocatalytic Performance. *Chem.—Eur. J.* **2012**, *18*, 10661–10668.
25. Chen, H.; Wang, N.; Di, J.; Zhao, Y.; Song, Y.; Jiang, L. Nanowire-in-Microtube Structured Core/Shell Fibers *via* Multifluidic Coaxial Electrospinning. *Langmuir* **2010**, *26*, 11291–11296.
26. Reddy, M. V.; Rao, G. V. S.; Chowdari, B. V. R. Metal Oxides and Oxysalts as Anode Materials for Li Ion Batteries. *Chem. Rev.* **2013**, *113*, 5364–5457.
27. Zhu, X.; Song, X.; Ma, X.; Ning, G. Enhanced Electrode Performance of Fe_2O_3 Nanoparticle-Decorated Nanomesh Graphene as Anodes for Lithium-Ion Batteries. *ACS Appl. Mater. Interfaces* **2014**, *6*, 7189–7197.
28. Xu, S.; Hessel, C. M.; Ren, H.; Yu, R.; Jin, Q.; Yang, M.; Zhao, H.; Wang, D. α-Fe_2O_3 Multi-Shelled Hollow Microspheres for Lithium Ion Battery Anodes with Superior Capacity and Charge Retention. *Energy Environ. Sci.* **2014**, *7*, 632–637.
29. Xu, X.; Cao, R.; Jeong, S.; Cho, J. Spindle-Like Mesoporous α-Fe_2O_3 Anode Material Prepared from MOF Template for High-Rate Lithium Batteries. *Nano Lett.* **2012**, *12*, 4988–4991.
30. Su, Q.; Xie, D.; Zhang, J.; Du, G.; Xu, B. *In Situ* Transmission Electron Microscopy Observation of the Conversion Mechanism of Fe_2O_3/Graphene Anode during Lithiation–Delithiation Processes. *ACS Nano* **2013**, *7*, 9115–9121.
31. Koo, B.; Xiong, H.; Slater, M. D.; Prakapenka, V. B.; Balasubramanian, M.; Podsiadlo, P.; Johnson, C. S.; Rajh, T.; Shevchenko, E. V. Hollow Iron Oxide Nanoparticles for Application in Lithium Ion Batteries. *Nano Lett.* **2012**, *12*, 2429–2435.
32. Wang, X.; Wu, X. L.; Guo, Y. G.; Zhong, Y.; Cao, X.; Ma, Y.; Yao, J. Synthesis and Lithium Storage Properties of Co_3O_4 Nanosheet-Assembled Multishelled Hollow Spheres. *Adv. Funct. Mater.* **2010**, *20*, 1680–1686.
33. Aldinger, F. Controlled Porosity by an Extreme Kirkendall Effect. *Acta Metall. Mater.* **1974**, *22*, 923–928.
34. Fan, H. J.; Knez, M.; Scholz, R.; Hesse, D.; Nielsch, K.; Zacharias, M.; Gösele, U. Influence of Surface Diffusion on the Formation of Hollow Nanostructures Induced by the Kirkendall Eeffect: The Basic Concept. *Nano Lett.* **2007**, *7*, 993–997.
35. Yin, Y.; Rioux, R. M.; Erdonmez, C. K.; Hughes, S.; Somorjai, G. A.; Alivisatos, A. P. Formation of Hollow Nanocrystals through the Nanoscale Kirkendall Effect. *Science* **2004**, *304*, 711–714.
36. Ferrari, A. C.; Robertson, J. Interpretation of Raman Spectra of Disordered and Amorphous Carbon. *Phys. Rev. B* **2000**, *61*, 14095–14107.
37. Dong, X.; Li, B.; Wei, A.; Cao, X.; Chan-Park, M. B.; Zhang, H.; Li, L. J.; Huang, W.; Chen, P. One-Step Growth of Graphene–Carbon Nanotube Hybrid Materials by Chemical Vapor Deposition. *Carbon* **2011**, *49*, 2944–2949.
38. Liang, J.; Jiao, Y.; Jaroniec, M.; Qiao, S. Z. Sulfur and Nitrogen Dual-Doped Mesoporous Graphene Electrocatalyst for Oxygen Reduction with Synergistically Enhanced Performance. *Angew. Chem., Int. Ed.* **2012**, *51*, 11496–11500.
39. Zheng, Z.; Wang, Y.; Zhang, A.; Zhang, T.; Cheng, F.; Tao, Z.; Chen, J. Porous Li_2FeSiO_4/C Nanocomposite as the Cathode Material of Lithium-Ion Batteries. *J. Power Sources* **2012**, *198*, 229–235.
40. Deng, D.; Kim, M. G.; Lee, J. Y.; Cho, J. Green Energy Storage Materials: Nanostructured TiO_2 and Sn-Based Anodes for Lithium-Ion Batteries. *Energy Environ. Sci.* **2009**, *2*, 818–837.
41. Reddy, M. V.; Yu, T.; Sow, C. H.; Shen, Z. X.; Lim, C. T.; Subba Rao, G. V.; Chowdari, B. V. R. α-Fe_2O_3 Nanoflakes as an Anode Material for Li-Ion Batteries. *Adv. Funct. Mater.* **2007**, *17*, 2792–2799.
42. Choi, S. H.; Kang, Y. C. Fe_3O_4-Decorated Hollow Graphene Balls Prepared by Spray Pyrolysis Process for Ultrafast and Long Cycle-Life Lithium Ion Batteries. *Carbon* **2014**, *79*, 58–66.
43. Xu, X.; Cao, R.; Jeong, S.; Cho, J. Spindle-like Mesoporous α-Fe_2O_3 Anode Material Prepared from MOF Template for High-Rate Lithium Batteries. *Nano Lett.* **2012**, *12*, 4988–4991.
44. Ye, J.; Zhang, J.; Wang, F.; Su, Q.; Du, G. One-Pot Synthesis of Fe_2O_3/Graphene and Its Lithium-Storage Performance. *Electrochim. Acta* **2013**, *113*, 212–217.
45. Zhu, X.; Zhu, Y.; Murali, S.; Stoller, M. D.; Ruoff, R. S. Nanostructured Reduced Graphene Oxide/Fe_2O_3 Composite as a High-Performance Anode Material for Lithium Ion Batteries. *ACS Nano* **2011**, *5*, 3333–3338.
46. Ji, L.; Lin, Z.; Alcoutlabi, M.; Toprakci, O.; Yao, Y.; Xu, G.; Li, S.; Zhang, X. Electrospun Carbon Nanofibers Decorated with Various Amounts of Electrochemically-Inert Nickel Nanoparticles for Use as High-Performance Energy Storage Materials. *RSC Adv.* **2012**, *2*, 192–198.
47. Gao, G.; Yu, L.; Wu, H. B. Hierarchical Tubular Structures Constructed by Carbon-Coated α-Fe_2O_3 Nanorods for Highly Reversible Lithium Storage. *Small* **2014**, *10*, 1741–1745.
48. Son, M. Y.; Hong, Y. J.; Lee, J. K.; Kang, Y. C. One-Pot Synthesis of Fe_2O_3 Yolk–Shell Particles with Two, Three, and Four Shells for Application as an Anode Material in Lithium-Ion Batteries. *Nanoscale* **2013**, *5*, 11592–11597.
49. Zhang, W. M.; Wu, X. L.; Hu, J. S.; Guo, Y. G.; Wan, L. J. Carbon Coated Fe_3O_4 Nanospindles as a Superior Anode Material for Lithium-Ion Batteries. *Adv. Funct. Mater.* **2008**, *18*, 3941–3946.
50. Zhao, Y.; Li, J.; Ding, Y.; Guan, L. Single-Walled Carbon Nanohorns Coated with Fe_2O_3 as a Superior Anode Material for Lithium Ion Batteries. *Chem. Commun.* **2011**, *47*, 7416–7418.
51. Han, F.; Li, D.; Li, W. C.; Lei, C.; Sun, Q.; Lu, A. H. Nanoengineered Polypyrrole-Coated Fe_2O_3@C Multifunctional Composites with an Improved Cycle Stability as Lithium-Ion Anodes. *Adv. Funct. Mater.* **2013**, *23*, 1692–1700.
52. Xu, Y.; Jian, G.; Liu, Y.; Zhu, Y.; Zachariah, M. R.; Wang, C. Superior Electrochemical Performance and Structure Evolution of Mesoporous Fe_2O_3 Anodes for Lithium-Ion Batteries. *Nano Energy* **2014**, *3*, 26–35.
53. Yin, Y.; Hu, Y.; Wu, P.; Zhang, H.; Cai, C. A Graphene–Amorphous $FePO_4$ Hollow Nanosphere Hybrid as a Cathode Material for Lithium Ion Batteries. *Chem. Commun.* **2012**, *48*, 2137–2139.
54. Liu, Y.; Xu, Y.; Han, X.; Pellegrinelli, C.; Zhu, Y.; Zhu, H.; Wan, J.; Chung, A. C.; Vaaland, O.; Wang, C. Porous Amorphous $FePO_4$ Nanoparticles Connected by Single-Wall Carbon Nanotubes for Sodium Ion Battery Cathodes. *Nano Lett.* **2012**, *12*, 5664–5668.
55. Choi, S. H.; Ko, Y. N.; Jung, K. Y.; Kang, Y. C. Macroporous Fe_3O_4/Carbon Composite Microspheres with a Short Li^+ Diffusion Pathway for the Fast Charge/Discharge of Lithium Ion Batteries. *Chem.—Eur. J.* **2014**, *20*, 11078–11083.
56. Qu, J.; Yin, Y. X.; Wang, Y. Q.; Yan, Y.; Guo, Y. G.; Song, W. G. Layer Structured α-Fe_2O_3 Nanodisk/Reduced Graphene Oxide Composites as High-Performance Anode Materials for Lithium-Ion Batteries. *ACS Appl. Mater. Interfaces* **2013**, *5*, 3932–3936.
57. Jeong, J. M.; Choi, B. G.; Lee, S. C.; Lee, K. G.; Chang, S. J.; Han, Y. K.; Lee, Y. B.; Lee, H. U.; Kwon, S.; Lee, G. Hierarchical Hollow Spheres of Fe_2O_3@Polyaniline for Lithium Ion Battery Anodes. *Adv. Mater.* **2013**, *25*, 6250–6255.
58. Rahman, M.; Wang, J. Z.; Hassan, M. F.; Wexler, D.; Liu, H. K. Amorphous Carbon Coated High Grain Boundary Density

Dual Phase $Li_4Ti_5O_{12}$-TiO_2: A Nanocomposite Anode Material for Li-Ion Batteries. *Adv. Energy Mater.* **2011**, *1*, 212–220.
59. Wu, Y. P.; Rahm, E.; Holze, R. Carbon Anode Materials for Lithium Ion Batteries. *J. Power Sources* **2003**, *114*, 228–236.
60. Larcher, D.; Masquelier, C.; Bonnin, D.; Chabre, Y.; Masson, V.; Leriche, J. B.; Tarascon, J. M. Effect of Particle Size on Lithium Intercalation into α Fe_2O_3. *J. Electrochem. Soc.* **2003**, *150*, A133–A139.
61. Guo, B.; Wang, X.; Fulvio, P. F.; Chi, M.; Mahurin, S. M.; Sun, X. G.; Dai, S. Soft-Templated Mesoporous Carbon-Carbon Nanotube Composites for High Performance Lithium-Ion Batteries. *Adv. Mater.* **2011**, *23*, 4661–4666.
62. Ko, Y. N.; Park, S. B.; Jung, K. Y.; Kang, Y. C. One-Pot Facile Synthesis of Ant-Cave-Structured Metal Oxide–Carbon Microballs by Continuous Process for Use as Anode Materials in Li-Ion Batteries. *Nano Lett.* **2013**, *13*, 5462–5466.
63. Won, J. M.; Choi, S. H.; Hong, Y. J.; Ko, Y. N.; Kang, Y. C. Electrochemical Properties of Yolk-Shell Structured $ZnFe_2O_4$ Powders Prepared by a Simple Spray Drying Process as Anode Material for Lithium-Ion Battery. *Sci. Rep.* **2014**, *4*, 5857–5860.
64. Hong, Y. J.; Son, M. Y.; Kang, Y. C. One-Pot Facile Synthesis of Double-Shelled SnO_2 Yolk-Shell-Structured Powders by Continuous Process as Anode Materials for Li-ion Batteries. *Adv. Mater.* **2013**, *25*, 2279–2283.
65. Lee, S. M.; Choi, S. H.; Kang, Y. C. Electrochemical Properties of Tin Oxide Flake/Reduced Graphene Oxide/Carbon Composite Powders as Anode Materials for Lithium-Ion Batteries. *Chem.—Eur. J.* **2014**, *20*, 15203–15207.
66. Li, N.; Liu, G.; Zhen, C.; Li, F.; Zhang, L.; Cheng, H. M. Battery Performance and Photocatalytic Activity of Mesoporous Anatase TiO_2 Nanospheres/Graphene Composites by Template-Free Self-Assembly. *Adv. Funct. Mater.* **2011**, *21*, 1717–1722.